Nanoscale Advances

ROYAL SOCIETY OF CHEMISTRY

PAPER

View Article Online
View Journal | View Issue

Check for updates

Cite this: *Nanoscale Adv.*, 2022, **4**, 1394

A sustainable one-step strategy for highly graphitized capacitive carbons with hierarchical micro–meso–macro porosity

Huili Liu, Suisui Su, Heng Wang, Miaomiao Wang, Shouren Zhang, Binbin Chang * and Baocheng Yang*

Large micropore surface area, superior electrical conductivity and suitable pore size are simultaneously desired characteristics for high-performance capacitive carbons. However, these desired features tend to be mutually competing, and are generally difficult to integrate into a single carbon. Considering this challenge, we developed a sustainable, less time-demanding, pollution-free strategy to construct highly graphitized porous carbon (GPC) by one-step heat-treatment. This approach achieves the need of the abovementioned characteristics for capacitive carbons, wherein potassium ferrate works as both an activating agent and graphitization catalyst to achieve synchronous hierarchical porosity and graphitization of wasted natural wood, and the resultant carbon materials possess a large micropore surface area of 870.4 m^2 g^{-1}, a highly graphitic carbon skeleton and a well-interconnected micro–meso–macropore structure. The assembled GPC-based symmetrical capacitors exhibited a satisfactory capacitive performance in different aqueous electrolytes (H_2SO_4, KOH and Na_2SO_4), including high specific capacitance, prominent rate capability, satisfactory energy density and good cycle stability. Meanwhile, we compared the contributions of porosity and the graphitized structure to capacitive performance, and porosity was dominant in determining capacitance and the graphitized skeleton had a positive effect in enhancing the capacitive performance. In addition, we established the relationship between the structure of GPC and electrochemical capacitive performance in different aqueous electrolytes, providing a valuable reference for GPC-based supercapacitors in different practical applications. More importantly, this strategy holds great promise to sustainably convert biowaste to high-added-value capacitive carbons for advanced energy storage applications in the future.

Received 8th December 2021
Accepted 11th January 2022

DOI: 10.1039/d1na00856k

rsc.li/nanoscale-advances

Open Access Article. Published on 12 January 2022. Downloaded on 1/21/2026 7:43:06 PM.
This article is licensed under a Creative Commons Attribution-NonCommercial 3.0 Unported Licence.

1. Introduction

Carbon-based electric double-layer capacitors (EDLCs), as a sustainable and efficient energy storage device, have drawn extensive attention owing to their unique advantages, including fast charge–discharge, high power density, simple principle, long cycle life and environmental friendliness.[1–5] Energy storage of EDLCs arises from the pure electrostatic charge accumulation on the surface of electrodes. Based on such a charge storage mechanism, the surface properties and pore structure play a vital role in determining the electrochemical capacitive performance of carbon-based EDLCs. Increasing the surface area and tailoring the pore size of capacitive carbon materials have been demonstrated to be valid strategies to enhance the capacitance.[6,7] Meanwhile, a certain amount of mesopores and macropores is beneficial for the transfer of electrolyte ions,[8,9] resulting in the improvement of capacitive performance, especially rate capability. In principle, it has been certified that porous carbons with abundant supermicropores are the best option for high-performance EDLCs, which is attributed to the matched size of the electrolyte ions (0.7–1.0 nm).[10,11] Consequently, microporous carbons with an optimized pore structure and a suitable proportion of mesopores and macropores are promising electrodes for high-efficiency carbon-based EDLCs.

On the other hand, superior electrical conductivity is also essential for carbon electrodes to enhance their capacitive performance, which can ensure rapid and efficient electron transport.[12–14] Construction of a graphitic skeleton is often used to enhance the electrical conductivity. According to the above theoretical analysis, hierarchically porous graphitic carbons are ideal candidates for high-performance carbon-based EDLCs owing to their unique features of combining good conductivity and superior porosity as well as suitable proportions of meso/macropores. Currently, porous graphitic carbons are synthesized by means of template methods, chemical/physical activation methods combining high-temperature treatment or catalytic graphitization.[15–18] Unfortunately, these strategies are

Henan Key Laboratory of Nanocomposites and Applications, Institute of Nanostructured Functional Materials, Huanghe Science and Technology College, Zhengzhou, Henan 450006, China. E-mail: binbinchang@infm.hhstu.edu.cn; baochengyang@infm.hhstu.edu.cn

© 2022 The Author(s). Published by the Royal Society of Chemistry

Open Access Article. Published on 12 January 2022. Downloaded on 1/21/2026 7:43:06 PM.
This article is licensed under a Creative Commons Attribution-NonCommercial 3.0 Unported Licence.

usually time-consuming and involve high-energy-consumption; meanwhile they need expensive templates and a combination of multiple activating agents, which is a two-step or multi-step process, seriously limiting their large-scale utilization and further development. Moreover, the superior microporosity usually lowers the electronic conductivity, and thus these desired characteristics are incompatible and even tend to be mutually competing in a single carbon material.[8,19] Hence, it is significantly desirable to develop a simple and effective approach for graphitic porous carbons with hierarchical micro–meso–macro porosity to offer multiple synergistic effects of the above-mentioned beneficial features for the best electrochemical capacitive performance.

Electrolytes are another key component of carbon-based EDLCs, which also have a great effect on the electrochemical performance of capacitors, especially in practical applications.[20,21] Consequently, the adopted electrolytes and carbon electrode materials mainly determine the overall electrochemical performance of capacitors. In order to provide a valuable reference for meeting the different demands of carbon-based EDLCs in practical applications, it is essential to establish the relationship between the structure of graphitized hierarchical porous carbons and their capacitive performance in different electrolytes.

To address these issues, we developed a simple one-step strategy by utilizing potassium ferrate (K_2FeO_4) to achieve the synchronous activation and graphitization of wasted natural wood for the preparation of graphitized porous carbon (GPC). K_2FeO_4 functions as both a porogen and graphitization catalyst to convert waste wood into high value-added capacitive carbon materials. The whole process is simple, sustainable, low-energy consuming and pollution-free without the addition of any toxic substance. The resultant GPC exhibited improved porosity of high-density micropores and well-proportioned meso/macropores, a multiscale pore size and a high graphitization degree, showing well balanced incompatible features in a single porous carbon. Benefiting from the well-interconnected conductive network and suitable multiscale pore sizes, the GPC material presented a prominent electrochemical capacitive performance, including large specific capacitance, satisfactory energy density and superior cycle stability. Meanwhile, we analyzed the nature behind the difference in the electrochemical capacitive properties of the GPC electrode in various aqueous electrolytes, and established the relationship between the structure of GPC and its electrochemical capacitive performance in different electrolytes, which would give a valuable reference for its potential practical application in different system GPC-based EDLCs. Importantly, our proposed approach shows great potential to achieve sustainable and large-scale utilization of biowaste for the production of high-value-added porous carbon electrodes in future energy storage applications.

2. Experimental section

2.1 Preparation of materials

Waste wood was collected and cut into pieces, washed repeatedly with deionized water, and then immersed in ethanol for 12 h. Subsequently, the materials were washed thoroughly with deionized water and dried at 80 °C overnight. The dried waste wood materials were then pre-carbonized at 400 °C for 2 h under an argon atmosphere with a ramp rate of 5 °C min^{-1}. The obtained dark solid product was ground to powder and denoted as wood carbon (WC). 3 g of WC powder was dispersed in 60 mL of K_2FeO_4 aqueous solution (0.1 M) under continuous stirring for 8 h, and the solution was evaporated to dryness on a rotary evaporator. Then, the obtained mixture was heat-treated at 900 °C for 2 h in an argon atmosphere with a heating rate of 5 °C min^{-1}. The carbonized sample was washed with diluted hydrochloric acid to remove residual inorganic impurities and further washed with deionized water to neutrality. Finally, the products were dried at 80 °C overnight to obtain graphitized porous carbon, which was denoted as GPC.

For comparison, 3.0 g of WC powder was respectively dispersed in 60 mL of KOH aqueous solution (0.2 M) and $FeCl_3$ solution (0.1 M) with continuous stirring for 8 h, and the solution was evaporated to dryness on a rotary evaporator. A subsequent process was carried out under the same experimental conditions as described above. The obtained samples were collected, washed and dried at 80 °C, and named PC and GC, respectively.

2.2 Characterization

X-ray diffraction (XRD) patterns were obtained on a Bruker D8 diffractometer using Cu Kα radiation ($\lambda = 0.15418$ nm) as an X-ray source. Nitrogen adsorption–desorption isotherms were obtained at −196 °C using a Micromeritics ASAP 2020HD88 analyzer. Before adsorption, the samples were out-gassed at 200 °C for 12 h. The specific surface area (S_{BET}) was evaluated using the Brunauer–Emmett–Teller (BET) method, the pore size distributions were calculated using the density functional theory (DFT) method, and the micropores were analyzed using the t-plot method. The morphology was observed on a FEI Tecnai G2 20 transmission electron microscope (TEM) with an accelerating voltage of 200 kV and on a scanning electron microscope (SEM, Quanta 250 FEG). Fourier transform infrared spectroscopy (FTIR) spectra of the sample in KBr pellet were recorded on a Thermo scientific Nicolet IS5 spectrometer. Raman spectra were recorded on a Raman spectrometer (WITEC Spectra Pro 2300I) with a 532 nm laser. The conductivity of materials was tested by using a four-point probe (RST-9). X-ray photoelectron spectra (XPS) were obtained on a VG ESCALAB MK II X-ray photoelectron spectrometer with an excitation source of Mg Kα (1253.6 eV).

2.3 Electrochemical measurements

The working electrodes were prepared by mixing the active material, carbon black and polytetrafluoroethylene (PTFE) binder with a weight ratio of 8 : 1 : 1. Then, the as-prepared slurry was coated on one side of nickel foam (1 cm × 1 cm) or carbon paper (1 cm × 1 cm), and dried at 80 °C in a vacuum overnight. After pressing it under 10 MPa for 60 s, the working electrode was obtained. The mass of active material loading in each working electrode was about 3–5 mg cm^{-2}. In a three-

Open Access Article. Published on 12 January 2022. Downloaded on 1/21/2026 7:43:06 PM.
This article is licensed under a Creative Commons Attribution-NonCommercial 3.0 Unported Licence.

electrode test, platinum foil and a Hg/HgO electrode were employed as counter and reference electrodes, respectively. All measurements including cyclic voltammetry (CV), galvanostatic charge/discharge (GCD), and electrochemical impedance spectroscopy (EIS) were performed on a CHI 760E electrochemical workstation at room temperature using H_2SO_4 (1 M), KOH (6 M) and Na_2SO_4 (0.5 M) as electrolytes. The EIS measurements were conducted in the frequency range of 10^{-2} to 10^5 Hz at the open circuit voltage. The gravimetric specific capacitance, C_{sp} (F g^{-1}) was calculated according to the following equation:

$$C_{sp} = \frac{I\Delta t}{m\Delta V} \quad (1)$$

where I (A) is the constant current, Δt (s) refers to the discharge time, m (g) represents the mass of active materials in the working electrode, and ΔV (V) expresses the potential range excluding the *IR* drop during the discharge process.

2.4 Fabrication of symmetric supercapacitors

A symmetric supercapacitor was assembled from two nearly identical working electrodes using glass fibre as the separator, wherein H_2SO_4 (1 M), KOH (6 M) and Na_2SO_4 (0.5 M) were used as electrolytes. The electrochemical behaviors of the symmetrical supercapacitors were assessed by the similar electrochemical technology described in the three-electrode system. The gravimetric specific capacitance, C_{sp} (F g^{-1}) for a single electrode was calculated from each galvanostatic charge–discharge curve according to the following equation:

$$C_{sp} = \frac{4I\Delta t}{m\Delta V} \quad (2)$$

where I (A) is the constant current, Δt is the discharge time (s), m (g) is the total mass of both electrodes, and ΔV (V) is the voltage change.

The energy density (E, W h kg^{-1}) was estimated by using the following formula:

$$E = \frac{1}{8}C_{sp}V^2 \quad (3)$$

The power density (P, W kg^{-1}) was calculated using the following equation:

$$P = \frac{E}{t} \quad (4)$$

where C_{sp} (F g^{-1}) is the specific capacitance of a single electrode, V (V) is the voltage change during the discharge process, and t (s) is the discharge time.

3. Results and discussion

3.1 The formation mechanism of the GPC material

Scheme 1 schematically illustrates the fabrication process of graphitized porous carbon *via* a one-step heat-treated route, wherein K_2FeO_4 was employed as an activating agent (K) and catalyst (Fe species) to achieve synchronous carbonization, pore-formation and graphitization of waste wood. During the impregnation process, K_2FeO_4 was hydrolyzed into KOH and $Fe(OH)_3$, according to eqn (5):

$$4K_2FeO_4 + 10H_2O \rightarrow 8KOH + 4Fe(OH)_3 + 3O_2 \quad (5)$$

In the following heat-treatment, KOH functions as a chemical activating agent to react with carbon, leading to abundant hierarchical pores. Fe species work as a graphitization catalyst to produce the graphitic carbon skeleton. But, these reaction processes did not proceed in a sequential order.[22,23]

With respect to the KOH activation, the reactions began with solid–solid reactions and then solid–liquid reactions, which involve the reduction of K compounds, the oxidation of C and other reactions among various active intermediates.[24] The detailed reaction equations of KOH activation are listed as follows:

$$6KOH + 2C \rightarrow 2K + 3H_2 + 2K_2O_3$$

$$K_2Co_3 + 2C \rightarrow 2K + 3CO$$

$$K_2Co_3 \rightarrow K_2O + CO_2$$

$$CO_2 + C \rightarrow 2CO$$

$$K_2O + C \rightarrow 2K + CO$$

For graphitization, amorphous Fe species ($Fe(OH)_3$) were first transformed into Fe_2O_3 at ~400 °C, and then further reduced to Fe_3O_4 by C or reductive gases (H_2 and CO) at elevated temperatures of 500–700 °C.[25] Fe_3O_4 was finally reduced to metallic Fe, which worked as a catalyst for the conversion of amorphous carbon into graphitic carbon.[26] The related reactions of Fe catalytic graphitization are described using the following equations:

$$Fe(OH_3) \rightarrow FeO(OH) \rightarrow Fe_2O_3$$

$$3Fe_2O_3 + (C, H_2, CO) \rightarrow 2Fe_3O_4 + (H_2O, CO, CO_2)$$

$$Fe_3O_4 + 4(C, H_2, CO) \rightarrow 3Fe + 4(H_2O, CO, CO_2)$$

Additionally, the voids remaining after the removal of potassium compounds and Fe species could contribute some additional mesopores and even macropores, resulting in the interconnected micro–meso–macro hierarchical porosity in the internal structure of GPC.

To verify the reasonability of the above proposed K_2FeO_4 activation process, the XRD pattern of the intermediate was recorded. After heat-treatment at 900 °C and before acid washing, the characteristic diffraction peaks of K_2CO_3, K_2O and metallic K can be observed (Fig. 1a), manifesting the occurrence of the KOH activation. The strong diffraction peaks at 2θ = 44.6°, 64.9° and 82.3° are assigned to metallic Fe (JCPDS no. 06-0696), suggesting the existence of a graphitization catalyst, which should be from the reduction of Fe^{3+} by carbon or reductive gases in the heat-treatment process. Moreover, the

© 2022 The Author(s). Published by the Royal Society of Chemistry

Open Access Article. Published on 12 January 2022. Downloaded on 1/21/2026 7:43:06 PM.
This article is licensed under a Creative Commons Attribution-NonCommercial 3.0 Unported Licence.

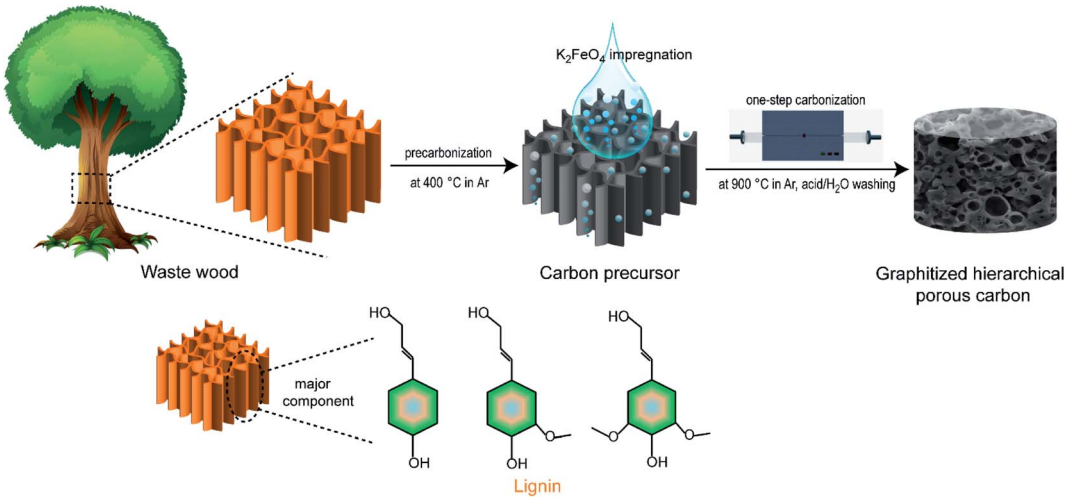

Scheme 1 Schematic illustration of the preparation of graphitized hierarchical porous carbon *via* a one-step strategy.

distinct diffraction peak at a 2θ value of 26.4° corresponds to typical (002) reflection of graphitic carbon, revealing the occurrence of Fe catalyzed graphitization for the wood carbon skeleton. Based on such XRD results, the above proposed K_2FeO_4 activation mechanism with synchronous pore-formation and skeleton graphitization is reasonable.

3.2 Structure and morphology characterization

The crystallographic structure and graphitization degree of all the as-obtained samples were further characterized by XRD and Raman spectroscopy. The characteristic diffraction peaks of K or Fe metal salt/oxide cannot be found in all the XRD patterns of the samples (Fig. 1b), indicating that these intermediate phases have been completely removed by acid washing. The XRD pattern of PC shows two weak hump-like diffraction peaks at 2θ angles range of 20–30 and 40–50°, suggesting the typical amorphous carbon framework.[27] For the GC sample, a weak peak of graphitic carbon (002) could be found, suggesting an enhanced graphitization degree, which should result from the destruction of the inherent structure by $FeCl_3$ catalyzed graphitization. For GPC, a sharp and strong diffraction peak of

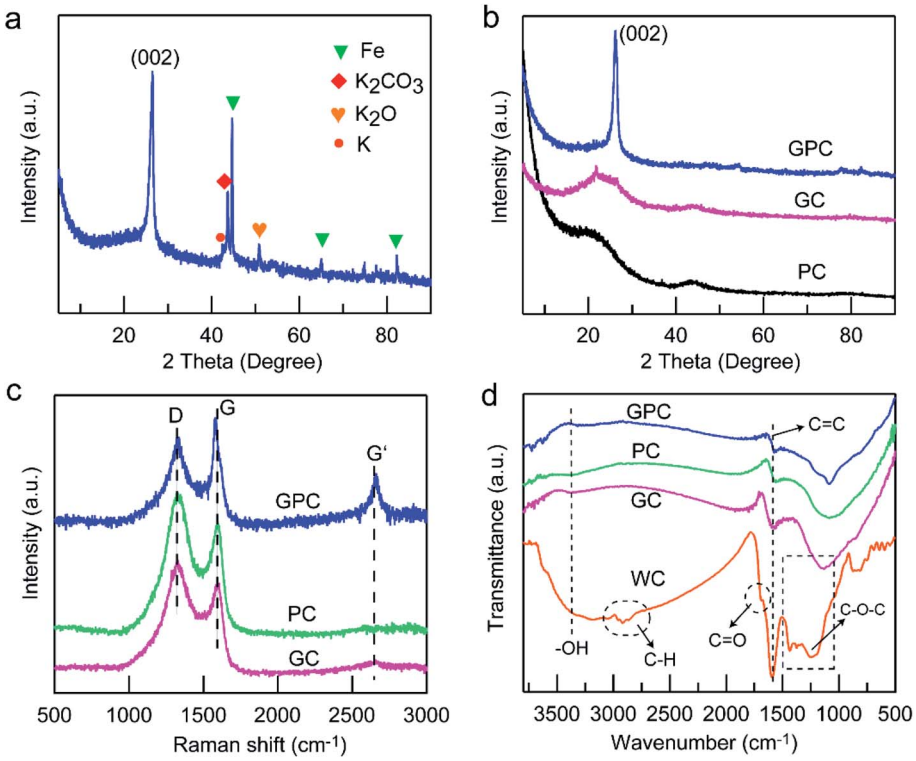

Fig. 1 Characterization of the resultant materials. (a) The XRD pattern of GPC before acid washing. (b) The XRD patterns of PC, GC and GPC. (c) Raman spectra of PC, GC and GPC. (d) The FTIR spectra of WC, PC, GC and GPC samples.

Open Access Article. Published on 12 January 2022. Downloaded on 1/21/2026 7:43:06 PM.
This article is licensed under a Creative Commons Attribution-NonCommercial 3.0 Unported Licence.

graphitic carbon (002) plane centered at $2\theta = 26.4^\circ$ can be clearly observed, indicative of a nearly perfect graphitized carbon framework,[28] which should be attributed to the synergistic effect of KOH activation and Fe catalytic graphitization on the carbon skeleton. Based on such XRD results, good crystallinity can be achieved in the one-pot synthesized GPC. Raman spectra were analyzed to further identify the graphitic structure of PC, GC and GPC samples (Fig. 1c). Two obvious peaks at ~1340 and ~1590 cm^{-1} can be found for all the samples, which correspond to the D- and G-band, respectively. The D-band is related to the disordered structure caused by carbon lattice defects, and the G-band reflects the ordered sp^2-bonded graphitic carbon structure.[29] Noticeably, an additional peak located at around 2680 cm^{-1} in the GPC sample is defined as the G′-band, which is a typical symbol of highly ordered graphitic carbon lattices.[30] Furthermore, the ratio of the relative intensity of D- and G-bands (I_D/I_G) is usually used to evaluate the degree of crystallization or defect density of carbon materials. In general, the narrower G-band and the lower I_D/I_G value reflect a higher graphitization degree. The I_D/I_G values of PC, GC and GPC are 1.24, 1.12 and 0.91, respectively, suggesting a higher and higher graphitization degree. In addition, GPC shows narrower D and G-bands and an intense G′-band than those of PC and GC, which confirms the conversion of the amorphous carbon skeleton of WC into graphitic carbon. Such results are consistent with the XRD analysis result. The conductivity of GPC is 6.8 S cm^{-1}, which is much higher than those of PC (2.6 S cm^{-1}) and GC (1.8 S cm^{-1}). Such superior conductivity of GPC should be attributed to its higher graphitization degree, resulting in an improved electronic conductivity.

FTIR spectra were recorded to analyze the surface functional groups of waste wood and reveal the change of surface chemical properties (Fig. 1d). For the biomass precursor of WC, the bands at 1100–1500 cm^{-1} are related to the C–O–C stretching vibrations.[31] The absorption bands located at 1550–1600 cm^{-1} correspond to the C=C and C=O stretching vibrations.[32] The absorption band at ~2850 cm^{-1} is ascribed to the C–H stretching vibration, and the broad absorption band at 3000–3500 cm^{-1} is caused by the –OH stretching vibration from adsorbed H_2O.[33] Such results suggest that the carbon precursor possesses abundant oxygen- and hydrogen-containing functional groups assigned to lignin and hemicellulose, which favors the chemical activation generating rich porosity. Obviously, PC, GC and GPC samples present a similar and simple FTIR spectrum with only weak absorption peaks of C–O and C=C. The absorption bands of oxygen- and hydrogen-containing groups (such as C=O, C–O, C–H and –OH) obviously weaken and even disappear, which should be attributed to the etching by KOH activation and the Fe catalyst on the carbon skeleton, resulting in the decomposition of these components.

The chemical composition of the surface of the as-prepared materials was further determined by XPS analysis. XPS survey spectra (Fig. 2a) suggest that only C and O remained in GC, PC and GPC samples. Fitting the spectra to each element suggests that the resultant samples contain primarily carbon with a content of 83.41–91.87 at% and a small amount of oxygen with a content of 8.13–16.59 at% (Fig. 2b). The gradually decreased content of oxygen in GC, PC and GPC should have resulted from the different etching degrees of KOH and $FeCl_3$. Meanwhile, the suitable surface oxygen content contributes to the improvement

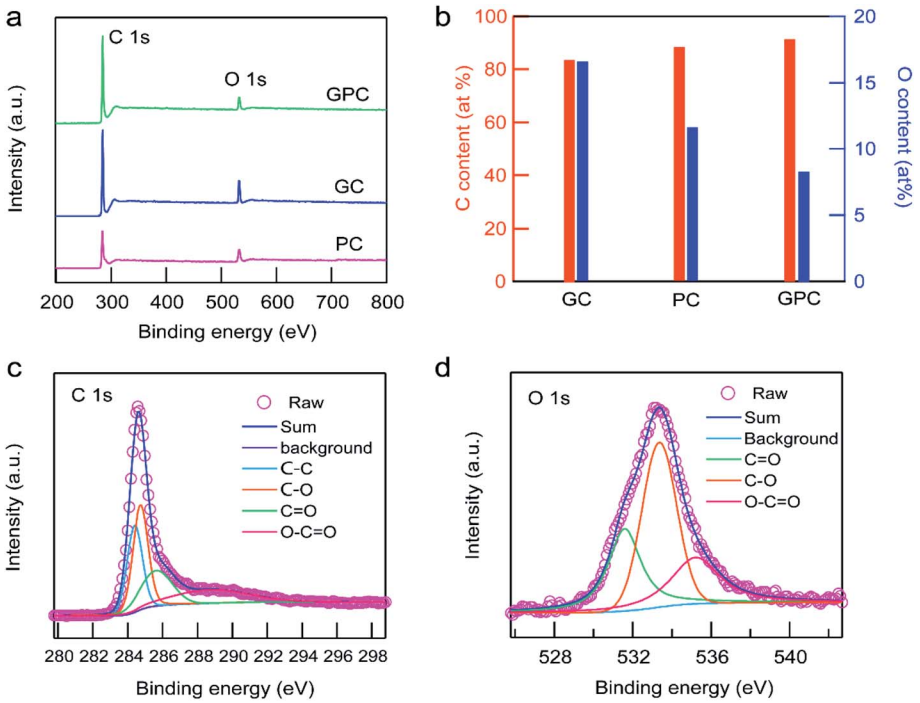

Fig. 2 XPS analysis. (a) The survey spectra. (b) C and O contents. (c) The high-resolution C 1s spectrum of the GPC sample. (d) The high-resolution O 1s spectrum of the GPC sample.

© 2022 The Author(s). Published by the Royal Society of Chemistry

Open Access Article. Published on 12 January 2022. Downloaded on 1/21/2026 7:43:06 PM.
This article is licensed under a Creative Commons Attribution-NonCommercial 3.0 Unported Licence.

of the electrochemical properties of carbonaceous materials.[34] The deconvolution of the C 1s spectrum reveals that the as-prepared carbon materials are composed of four types of carbon atoms. Taking the spectrum of C 1s of the GPC spectrum as an example, the high-resolution C 1s spectrum (Fig. 2c) could be deconvoluted into one sharp peak at 284.2 eV corresponding to graphitic C–C .[35] The other three peaks at 284.6, 285.7 and 289.5 eV are assigned to C–O, C=O and O–C=O, respectively.[36] The O 1s spectrum could be fitted into three peaks positioned at 531.6, 533.8 and 535.9 eV (Fig. 2d), which represents oxygen atoms in C=O, C–O and –O–C=O, respectively.[37] As a result, the relatively high oxygen content is beneficial to improve the surface hydrophilicity of carbon materials, enabling good accessibility of the electrolyte, resulting in an improved electrochemical capacitive storage capacity in aqueous electrolytes.

The evolution of the microstructure and morphology was revealed by SEM and TEM. The original WC precursor sample shows a regular microchannel structure arrayed in parallel with an average tube diameter of ~5–6 μm, and the surface is smooth with few pores (Fig. 3a). After only KOH activation, the PC sample basically retains the aligned microchannel structure inherited from the WC precursor (Fig. 3b). But some tubular fragments can be observed in the PC sample, which should be caused by KOH etching. The thickness of the channel walls is around 1 μm and abundant tiny pores are present on the walls, which is attributed to the KOH activation, resulting in the formation of pores. For only the $FeCl_3$ catalyst, the original regular microchannel microstructure of WC has been greatly damaged; the GC sample shows an irregular honeycomb-like block structure with numerous surface macroscopic pores of ~1 μm (Fig. 3c), which should be attributed to the corrosion of

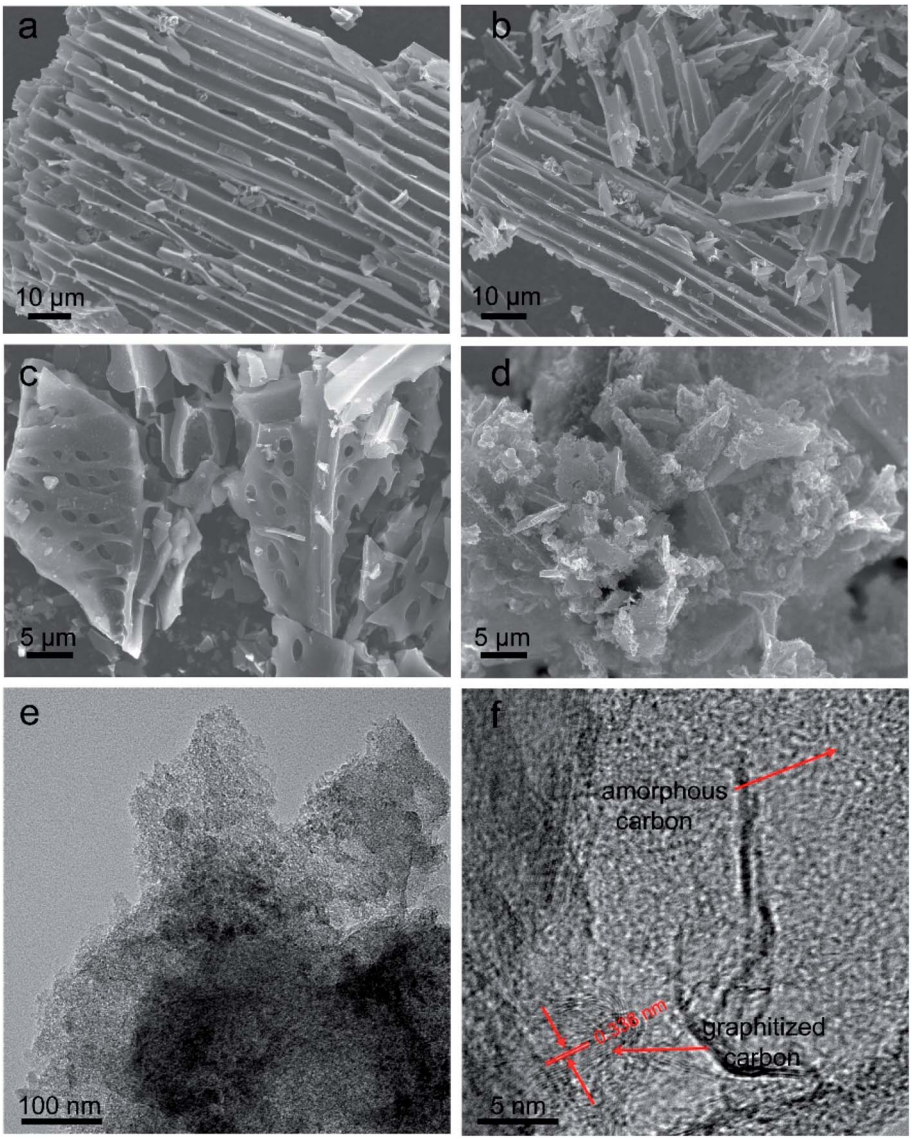

Fig. 3 Structure and morphology characterization. (a) SEM image of WC. (b) SEM image of PC. (c) SEM image of GC. (d) SEM image of GPC. (e) TEM image of GPC. (f) High-resolution TEM image of GPC.

Open Access Article. Published on 12 January 2022. Downloaded on 1/21/2026 7:43:06 PM.
This article is licensed under a Creative Commons Attribution-NonCommercial 3.0 Unported Licence.

$FeCl_3$ during the graphitization. After one-step synchronous carbonization and graphitization using K_2FeO_4, GPC displays an irregular particle shape with an interconnected hierarchical framework (Fig. 3d), which should be ascribed to the synergistic effect of KOH activation and Fe catalytic graphitization. Compared to the GC sample, the surface of GPC is rough and fluffy with plenty of nanopores. The continuous hierarchical pores of GPC can be further observed in the TEM image (Fig. 3e), and the interconnected micropores and small mesopores are discernible. In the high-resolution TEM image (Fig. 3f), the carbon skeleton of GPC is composed of an amorphous carbon structure and a short graphite layer with a distinct lattice distance of 0.338 nm, suggesting a considerably high degree of graphitization. Such a highly graphitized carbon framework favors the enhancement of conductivity and the improvement of charge transfer kinetics, resulting in superior electrochemical capacitive storage capacity.

N_2 adsorption–desorption measurements were performed to investigate the porosity of the PC, GC and GPC samples. GC and PC samples both exhibit a typical type I isotherm of the microporous structure (Fig. 4a), and the sharp adsorption inflection at low relative pressure manifests a prominent microporosity. Noticeably, the PC sample has a higher N_2 adsorption amount than that of the GC sample, meaning a larger micropore surface area, which should have resulted from the further KOH activation. The GPC sample exhibits a typical type I adsorption isotherm with a sharp adsorption inflection at a low relative pressure of <0.01 and a type IV isotherm with a H3 type hysteresis loop in the relative pressure range of 0.45–0.85 as well as an enhanced adsorbed amount at a high relative pressure of 0.9–1.0, indicative of the coexistence of micro–meso–macro hierarchical pores.[38] The hierarchical porosity can be further confirmed by the pore size distribution (Fig. 4b). Obviously, GC and PC samples both have a hierarchical micropore size, and the micropores of GC are mainly centered at 0.68 and 1.37 nm, and those of PC are mainly centered at 0.51–1.27 nm. The GPC sample exhibits a hierarchical porous structure with narrow ultramicropores of 0.58 nm, supermicropores of 1.19–1.69, mesopores of 2.63 and larger mesopores of 5–20 nm as well as the multiscale macropores. The detailed pore textural parameters of GC, PC and GPC samples are summarized in Table 1. It is easy to find that the activating agent KOH and the $FeCl_3$ catalyst have a significant influence on the structural characteristics of materials. When only the $FeCl_3$ catalyst is used, GC shows a low surface area and a small micropore volume. However, when only the activating agent KOH is used, the PC sample exhibits a higher surface area and a larger micropore volume, which validates that KOH is indeed an efficient activating agent to create a developed microporous structure. Due to the simultaneous activation and catalytic graphitization of K_2FeO_4, the GPC sample shows a high BET surface area with a suitable proportion of micro/mesoporosity and a unique micro–meso–macro hierarchical pore size.

Different from other highly corrosive activators, K_2FeO_4 is a relatively mild activating agent/catalyst, which can afford a high yield of porous graphitized carbon with a large surface area and a superior hierarchical porosity. Based on the above characterization results, the GPC sample exhibits some unique structural features: (i) the large accessible surface area could provide a large number of electroactive sites for ion accumulation and energy storage; (ii) the well-interconnected hierarchical porosity composed of appropriate micro–meso–macro pore size distribution promotes electrolyte penetration and shortens the ion diffusion distance; (iii) highly graphitized carbon skeleton ensures outstanding electrical conductivity for ion transport and rapid electron transfer. Benefiting from these advantageous characteristics, GPC is expected to be a promising electrode material for advanced EDLC storage devices.

3.3 Electrochemical capacitive storage capacity

To evaluate the advantages of GC, PC and GPC samples as electrodes for supercapacitors, the electrochemical capacitive performance of a single electrode was first investigated in various electrolytes by using a three-electrode system. The CV curves of GC, PC and GPC materials at a scan rate of 50 mV s^{-1} in H_2SO_4, KOH and Na_2SO_4 aqueous electrolytes are displayed in Fig. 5a–c, respectively. Obviously, the CV curves of all the carbon electrodes present a quasi-rectangular shape with a slight deformation in the three different aqueous electrolytes, demonstrating a dominant EDLC nature with a limited pseudocapacitive behavior from the surface functional groups.[39] The area of the encircled CV curve reflects the capacitance value, and the larger CV area means a higher specific capacitance, and thus GPC shows a better capacitive capacity than PC and GC. In H_2SO_4 electrolyte, the CV curves, especially for the GPC sample, show a set of broad redox peaks at around 0.5/0.2 V, which

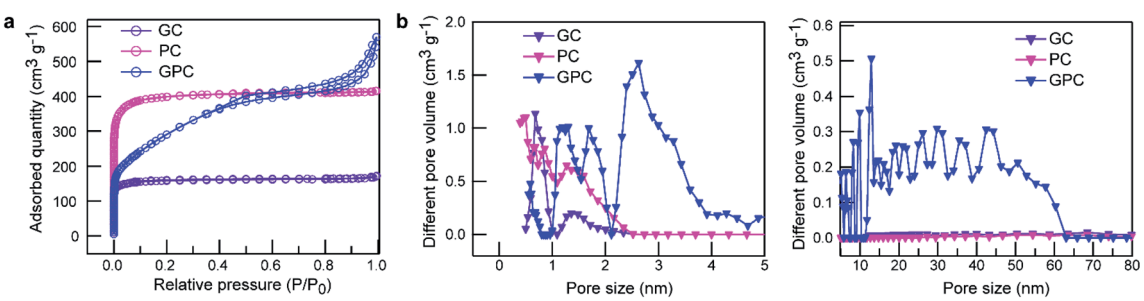

Fig. 4 Pore structure characterization. (a) N_2 adsorption–desorption isotherms and (b) pore size distribution of GC, PC and GPC.

© 2022 The Author(s). Published by the Royal Society of Chemistry

Open Access Article. Published on 12 January 2022. Downloaded on 1/21/2026 7:43:06 PM. This article is licensed under a Creative Commons Attribution-NonCommercial 3.0 Unported Licence.

Table 1 Pore textural properties of PC, GC and GPC samples

Sample	S_{BET} (m^2 g^{-1})	S_{micro} (m^2 g^{-1})	S_{meso} (m^2 g^{-1})	V_{total} (cm^3 g^{-1})	I_D/I_G
GC	630.1	619.9	10.2	0.27	1.12
PC	1575.8	1551.5	24.3	0.64	1.24
GPC	1257.7	870.4	387.3	0.89	0.91

indicates the existence of pseudocapacitive behavior from the oxidation/reduction of surface oxygen-containing groups (such as quinone groups). In KOH electrolyte, a slight hump peak appears at around −0.8 V in all the CV curves, which could arise from the pseudocapacitance related to the surface rich oxygen-containing species.[40] Similarly, a small tuber at around −0.2 V appears on the CV curves in neutral Na_2SO_4 electrolyte, which is related to the pseudo-faradaic reaction of surface quinone-like groups (C═O).[41] In addition, the CV curves of the GC sample in the three electrolytes are the smallest and distorted, meaning a poor capacitive capacity, which should have resulted from the poor porosity and high surface oxygen content, hindering ion transport. The GCD profiles of GC, PC and GPC samples at 1 A g^{-1} in H_2SO_4, KOH and Na_2SO_4 electrolytes are plotted in Fig. 5d–f, respectively. All the GCD curves exhibit a symmetric triangular shape, indicating an ideal EDLC feature and good electrochemical reversibility.[42] Noticeably, the GCD curves in H_2SO_4 electrolyte present a slightly obvious distortion with a tailing drag in the low potential region, which could be ascribed to the relatively more pseudocapacitance contribution from the surface oxygen-containing groups. Moreover, the GCP electrode shows the smallest *IR* drop in all three electrolytes, meaning the lowest internal resistance and fast electron transfer rate, which should be due to its highly graphitized carbon skeleton with a prominent hierarchical porosity. Since the discharge time represents the capacitance value, a longer discharge time corresponds to a larger specific capacitance value. As a result, the GPC sample exhibits the largest specific capacitance value, which is consistent with the result of the CV curves. The GPC electrode can achieve 354.8, 323.9 and 188.7 F

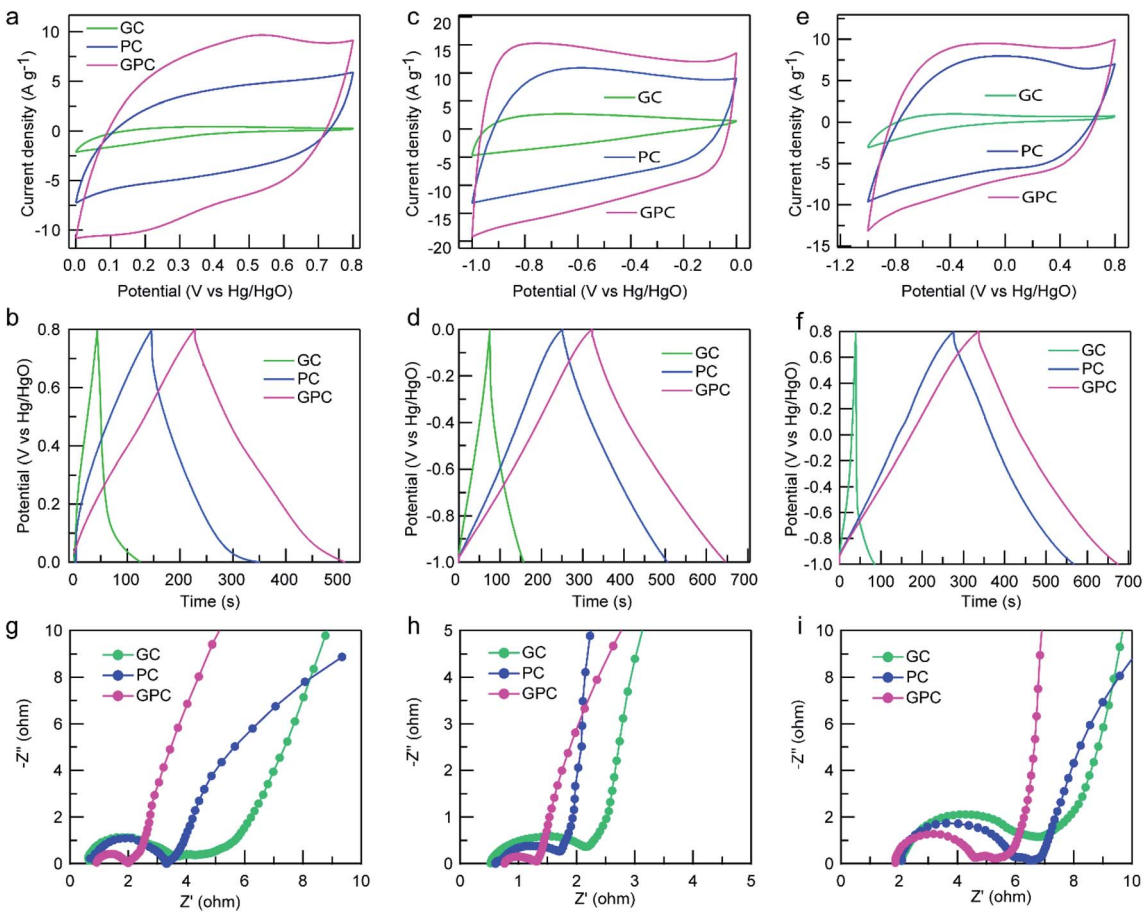

Fig. 5 Electrochemical capacitive behaviors of GC, PC and GPC in different electrolytes using a three-electrode system: CV curves at 50 mV s^{-1} in (a) 1 M H_2SO_4, (c) 6 M KOH and (e) 0.5 M Na_2SO_4. GCD profiles at 1 A g^{-1} in (b) 1 M H_2SO_4, (d) 6 M KOH and (f) 0.5 M Na_2SO_4. EIS analysis in (g) 1 M H_2SO_4, (h) 6 M KOH and (i) 0.5 M Na_2SO_4 electrolytes.

Open Access Article. Published on 12 January 2022. Downloaded on 1/21/2026 7:43:06 PM. This article is licensed under a Creative Commons Attribution-NonCommercial 3.0 Unported Licence.

g^{-1} in H_2SO_4, KOH and Na_2SO_4 aqueous electrolytes at 1 A g^{-1}, respectively, which are comparable and even higher than those of many previously reported biomass-derived porous carbon electrodes.[43–46] Based on the capacitive performance of GC, PC and GPC in different electrolytes, the PC electrode exhibits a higher capacitance value than that of the GC electrode, demonstrating that a superior porosity, especially a high microporosity, plays a crucial role in the capacitive performance of the material. Compared to the PC electrode, the GPC electrode shows better capacitive properties in spite of its decreased microporosity, which suggests that a highly graphitized carbon skeleton and a hierarchical porosity can promote the capacitive performance of the electrode. The remarkable capacitive performance of GPC should be ascribed to the following reasons: (i) its relatively large surface area provides more electroactive sites for ion accumulation and energy storage; (ii) its suitable proportion of micro/mesopores offers a more accessible surface area, improving the utilization rate of surface active sites; (iii) the well-interconnected hierarchical micro–meso–macropore size facilitates efficient ion diffusion; (iv) its nearly-perfect graphitized skeleton provides high electrical conductivity, favoring rapid electron transport.

EIS analysis was employed to further investigate the electrochemical capacitive performance of GC, PC and GPC electrodes in the three aqueous electrolytes (Fig. 5g–i). All of the Nyquist plots display a semicircle in the high frequency region and an almost vertical line in the low frequency region, implying a typical EDLC feature.[47] The high frequency semicircle stands for the charge transfer resistance (R_{ct}) of the electrodes. It is clear that the R_{ct} values of carbon electrodes in H_2SO_4 and KOH electrolytes are much smaller than that in Na_2SO_4, manifesting a more efficient ionic diffusion and smaller ion transport kinetics as well as a lower steric hindrance, which favors a better capacitive capacity. Furthermore, the *IR* drop values in Na_2SO_4 are slightly higher than those in H_2SO_4 and KOH electrolytes, suggesting a higher equivalent series resistance value, which is consistent with the results of EIS analysis.

With respect to GC, PC and GPC electrodes, it can be clearly found that their capacitance values in H_2SO_4 and KOH are much higher than those in Na_2SO_4, which should be related to the size of solvated electrolyte ions.[48] The size of solvated H^+ and K^+ ions is smaller than that of solvated Na^+ (Table 2),[49,50] which endows the higher ions acceptability by the pores in H_2SO_4 and KOH electrolytes, enabling better electrochemical capacitive storage performance. Based on the above capacitive results and related references,[49] the adsorption of different electrolyte ions on GPC with hierarchical pores is simulated (Fig. 6a). The macropores can serve as electrolyte ions reservoirs and transfer avenues, favoring electrolyte ions into the interior pores of GPC. Mesopores promote the accessibility of electrolyte ions by providing a wider transfer pathway for fast diffusion and migration of electrolyte ions, which favors high capacitance retention at fast charge–discharge rates. Micropores are the major ion adsorption sites for ion accumulation, which bring dominant contributions to capacitance. However, most micropores of small size would limit the supply of electrolyte ions with relatively large size, resulting in a limited enhancement of capacitance. The interconnected hierarchical pores with the spatial distribution of macropores, mesopores and micropores greatly facilitate the accessibility of GPC to electrolyte ions and the fast diffusion of numerous electrolyte ions. The electrochemical capacitive performance of carbon-based EDLCs depends not only on the effective pores and surfaces properties of porous carbons, but also on the match between the pore size of porous carbons and the size of electrolyte ions. It can be noted that different electrolyte ions can match different sized pores and surfaces of porous carbons, and act as adsorption sites for cations and anions, as presented in Fig. 6b–d. Solvated H^+ and K^+ with a smaller size can reach smaller size pores of GPC, and thus GPC has higher utilization for pores and surfaces in H_2SO_4 and KOH electrolytes, leading to higher capacitance values. The rate capability is more dependent on the capacity match between positive and negative electrodes, including the ion size and ionic conductivity. As a result, the GPC electrode exhibits a satisfactory rate capability in KOH and Na_2SO_4 electrolytes.

To further evaluate the effect of electrolytes on the practical capacitive performance of the GPC electrode for supercapacitor application, a symmetric supercapacitor cell was assembled, which is schematically illustrated in Fig. 7a. Two-electrode tests of the assembled GPC-based symmetric supercapacitors were performed in H_2SO_4, KOH and Na_2SO_4 electrolytes. Fig. 7b depicts CV curves of the symmetrical capacitor at various scan rates in H_2SO_4. A good symmetric CV curve can be observed when the scan rate increases from 5 to 50 mV s^{-1}, indicating a good ion reversible adsorption–desorption process during charge and discharge. A set of anodic and cathodic peaks are centered at 0.25/0.55 V, which are caused by the faradaic process of oxidation/reduction of quinone groups at the surface of the GPC material. Such results are consistent with the analysis results of the three-electrode test. Fig. 7c shows the GCD profiles of the assembled GPC-based symmetric supercapacitors at various current densities ranging from 0.5 to 8 A g^{-1} in H_2SO_4. All the GCD curves display a relatively symmetrical triangular shape with slight deformation, suggesting good capacitive performance and electrochemical reversibility. The slight deformation at low voltage could be related to the surface redox reaction, further confirming the existence of pseudocapacitance. With the increase of current density from 0.5 to 8 A g^{-1}, ~31.6% of capacitance retention can be obtained in H_2SO_4 (Fig. 7d), indicative of a relatively low rate capability, which could have resulted from the poor faradaic reaction of surface groups at high current density. The CV curves of the assembled GPC-based symmetric supercapacitor exhibit a typical rectangular shape in KOH electrolyte (Fig. 7e).

Table 2 The size of bare and solvated ions

	H^+	Na^+	K^+	SO_4^{2-}	OH^-
Bare ion radius (nm)	0.115	0.095	0.133	0.290	0.176
Solvated ion radius (nm)	0.280	0.358	0.331	0.379	0.300

© 2022 The Author(s). Published by the Royal Society of Chemistry

Open Access Article. Published on 12 January 2022. Downloaded on 1/21/2026 7:43:06 PM.
This article is licensed under a Creative Commons Attribution-NonCommercial 3.0 Unported Licence.

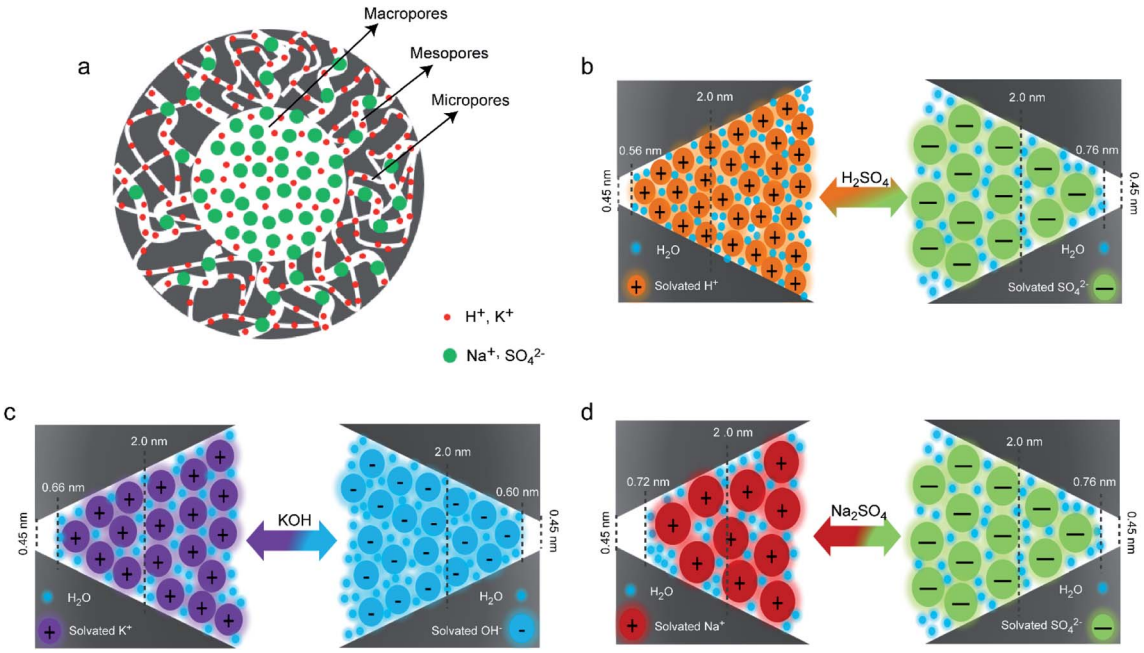

Fig. 6 (a) Diagram of electrolyte ion diffusion and adsorption in the hierarchical pores of GPC. Diagram of different solvated ions residing in hierarchical pores of GPC: (b) H_2SO_4; (c) KOH; (d) Na_2SO_4.

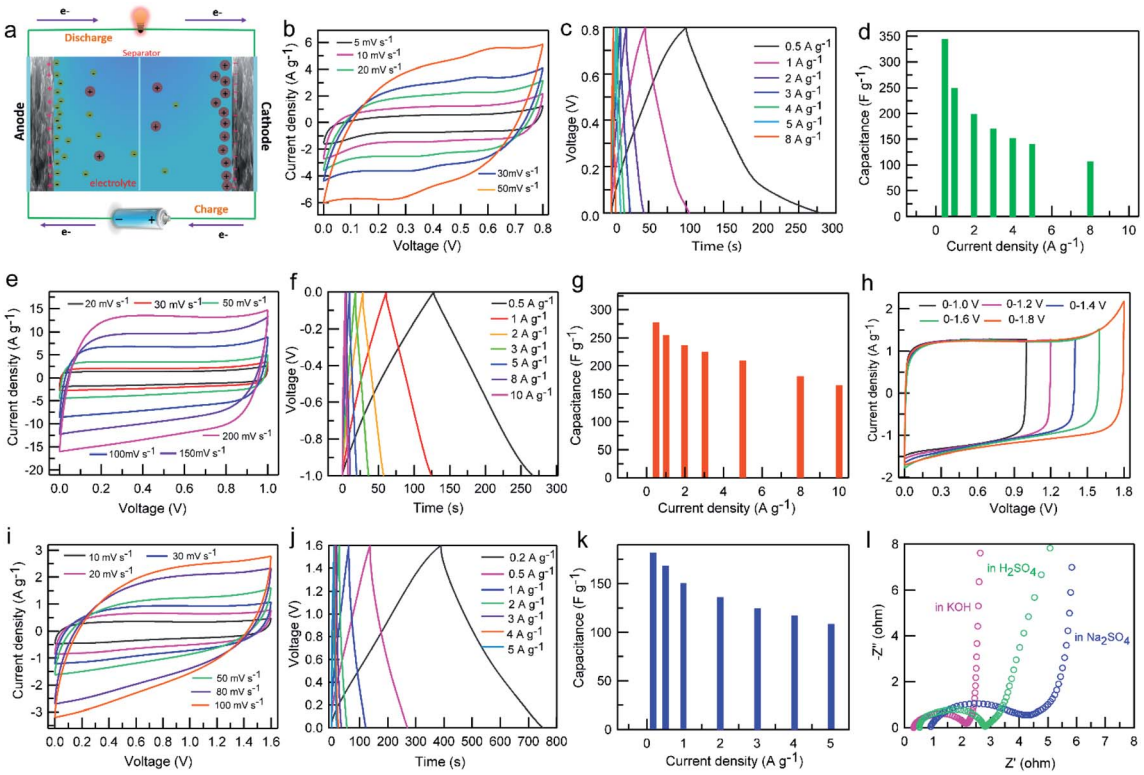

Fig. 7 (a) Schematic illustration of the GPC-based symmetric supercapacitor. Electrochemical capacitive behaviors of the GPC-based symmetric capacitor in 0.5 M H_2SO_4: (b) CV curves at various scan rates; (c) GCD profiles at various current densities; (d) capacitances *vs.* various current densities. Electrochemical capacitive behaviors of the GPC-based symmetric capacitor in 6 M KOH: (e) CV curves at different scan rates; (f) GCD curves at different current densities; (g) rate capability; electrochemical capacitive behaviors of the GPC-based symmetric capacitor in 0.5 M Na_2SO_4: (h) CV curves with different operating voltage windows at 50 mV s^{-1}; (i) CV curves at different scan rates; (j) GCD curves at different current densities; (k) rate capability; (l) Nyquist plot in various electrolytes.

Open Access Article. Published on 12 January 2022. Downloaded on 1/21/2026 7:43:06 PM.
This article is licensed under a Creative Commons Attribution-NonCommercial 3.0 Unported Licence.

With the increase of the scan rate from 20 to 200 mV s^{-1}, the CV curves still maintain the good rectangle-like shape, indicating superior transportability of electrons and ions as well as a good rate performance. The GCD curves display a symmetrical triangular shape with no obvious *IR* drops (Fig. 7f). Even when the current density increases to 10 A g^{-1}, the GCD curve is linearly symmetric, meaning an excellent reversible charge–discharge behavior. The specific capacitance values of the GPC-based symmetrical capacitor in KOH electrolyte at various current densities are summarized in Fig. 7g. A high capacitance value of 275.8 F g^{-1} at 0.5 A g^{-1} is achieved, and a satisfactory capacitance of 174.6 F g^{-1} is still retained at even 10 A g^{-1} with a capacitance retention of ~64%, suggesting a satisfactory rate capability, which is in line with the CV results.

A high operating voltage is vital for high energy density of supercapacitors in practical applications. Neutral electrolytes can withstand a higher operating voltage than acidic and alkaline electrolytes by reducing the possibility of inducing the water hydrolysis reaction because of either the hydrogen evolution reaction or oxygen evolution reaction.[21] Therefore, we employed a neutral Na_2SO_4 solution as electrolyte to assemble a GPC-based symmetric capacitor. As expected, the GPC electrode can withstand a voltage of 1.6 V or higher in the Na_2SO_4 electrolyte without a significant distortion of the anodic current (Fig. 7h). A voltage window of 0–1.6 V was chosen to assess the overall electrochemical capacitive performance of the GPC-based symmetric capacitor in Na_2SO_4 electrolyte. With the increase of the scan rate from 10 to 100 mV s^{-1}, the CV curves still maintain a good quasi-rectangular shape with no significant distortion (Fig. 7i), indicating superior rate capability. Meanwhile, the GCD profiles at various current densities from 0.2 to 5 A g^{-1} maintain a symmetric triangular shape (Fig. 7j), manifesting its excellent electrochemical reversibility. Based on the GCD curves, the GPC-based symmetric capacitor delivers a capacitance value of 176 F g^{-1} at 0.2 A g^{-1}, and importantly, it still achieves a capacitance 112 F g^{-1} at 5 A g^{-1} with a capacitance retention of ~64% (Fig. 7k). Obviously, the capacitance retention in Na_2SO_4 is significantly higher than those in the acidic and alkaline electrolytes at 5 A g^{-1}. As solvated Na^+ and SO_4^{2-} cannot enter smaller sized micropores, the ion adsorption sites need to be provided by mesopores and larger micropores. As a result, the ion transport distances of solvated Na^+ and SO_4^{2-} are greatly shortened, and thus greatly increase pore accessibility and accelerate the ion diffusion process. The high mesoporosity ratio of the GPC electrode is very favorable for its rate performance in Na_2SO_4 electrolyte.

EIS analysis was also carried out to evaluate the capacitive behavior of the GPC-based symmetric capacitor in aqueous electrolytes in a two-electrode system. The Nyquist plots of the GPC electrode in various electrolytes are almost perpendicular to the real axis in the low frequency region with a semicircle in the high frequency region (Fig. 7l), suggesting an ideal EDLC behavior. The order of the semicircular radius is as follows: KOH < H_2SO_4 < Na_2SO_4, indicating lower R_{ct} values in the KOH and H_2SO_4 electrolytes than that in the Na_2SO_4 electrolyte, which is consistent with the result of the three-electrode test. A typical 45° slope can be clearly observed in the Nyquist plot of the GPC electrode in the Na_2SO_4 electrolyte, which represents Warburg resistance, manifesting that the adsorption process of ions is limited by electrolyte diffusion. The above results demonstrate that the GPC electrode has better electronic conductivity in KOH and H_2SO_4 electrolytes than in Na_2SO_4 electrolyte.

The Ragone plots of the GPC-based symmetric supercapacitors in different electrolytes are shown in Fig. 8a. The highest energy densities obtained for GPC-based symmetric supercapacitors in H_2SO_4 and KOH electrolytes are 7.7 and 9.7 W h kg^{-1}, respectively. Such relatively low energy density should be related to the small operating voltage. Obviously, the GPC-based symmetric supercapacitor can deliver a high energy density of 16.3 W h kg^{-1} at a power density of 161.9 W kg^{-1} in neutral Na_2SO_4 electrolyte, which is nearly 2-fold higher than those in H_2SO_4 and KOH electrolytes. Importantly, the energy density of the GPC-based symmetric supercapacitor still remains as high as 9.6 W h kg^{-1} at 3760 W kg^{-1} in Na_2SO_4, which is superior to most of porous carbons.[51–54] Such satisfactory energy density should be benefited from its widened working voltage as high as 1.6 V. Moreover, the cycling stability of GPC-based symmetric supercapacitors in various aqueous electrolytes was tested in a two-electrode system (Fig. 8b). The results show that the assembled GPC-based symmetric supercapacitors are excellently stable in the three aqueous electrolytes, and the 94.8, 93.2 and 92.1% capacitance retentions are respectively obtained after consecutive 10 000 charge–discharge cycles at a current density of 1 A g^{-1} in KOH, H_2SO_4 and Na_2SO_4 electrolytes. As an application demonstration, we assembled GPC-based symmetrical devices in series in Na_2SO_4 electrolyte which power a LED bulb brightly (Fig. 8c) and sustain a lit LED for about 80 s (Fig. 8d).

3.4 The effect of electrolytes on the electrochemical capacitive properties of the GPC electrode

Considering the different requirements for symmetric capacitors in practical applications, we compared the effect of electrolytes on electrochemical capacitive behaviors of the GPC electrode in the following six aspects: capacitance, rate capability, energy density, conductivity, cycle stability and operating voltage. As displayed in Fig. 8e, the electrochemical capacitive performance is better and better from inside to outside. The outer region represents better performance. The capacitance values of the GPC-based symmetric capacitor in KOH and H_2SO_4 electrolytes are dominant, mainly benefiting from the smaller size of solvated H^+ and K^+ ions. The lowest capacitance of the GPC electrode was observed in Na_2SO_4, which is because of the less effective pores and surface caused by the large size of solvated Na^+ and SO_4^{2-} ions. However, the rate capability of the GPC electrode in Na_2SO_4 is satisfactory, which is mainly a result of the shorter ion transport distances of Na^+ and SO_4^{2-} ions to the surface of the GPC electrode. The rate capability of the GPC-based symmetric capacitor in KOH is also good owing to the small steric hindrance and fast ion mobility rate of K^+ and OH^- ions. Furthermore, as a compensation of the low capacitance of the GPC-based symmetric capacitor, a higher energy density is

© 2022 The Author(s). Published by the Royal Society of Chemistry

Open Access Article. Published on 12 January 2022. Downloaded on 1/21/2026 7:43:06 PM.
This article is licensed under a Creative Commons Attribution-NonCommercial 3.0 Unported Licence.

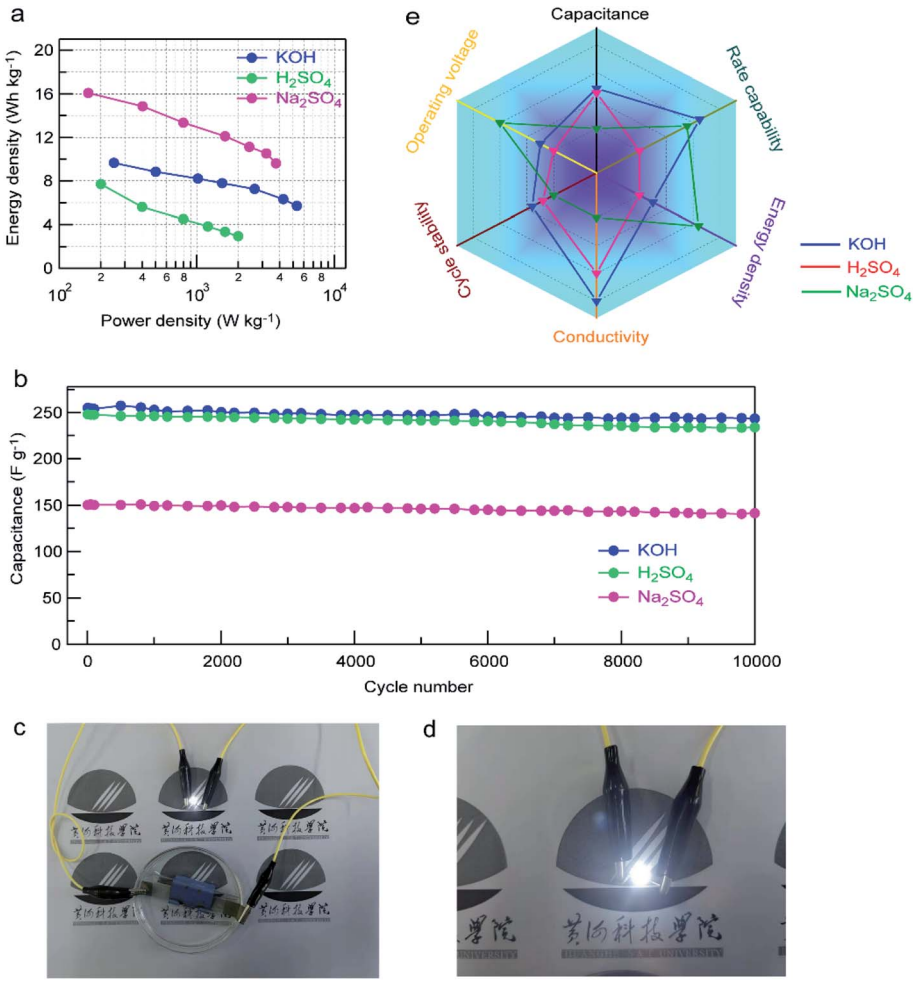

Fig. 8 (a) Ragone plots of the GPC-based symmetric supercapacitor in different electrolytes. (b) The cycle stability of the GPC electrode at 1 A g^{-1} in different electrolytes. (c and d) The photograph of a LED lamp powered by the two symmetric capacitors in series. (e) The comparison of the electrochemical performance of the GPC electrode in different electrolytes.

achieved in Na_2SO_4 electrolyte, which should be due to its higher working voltage of 1.6 V. The GPC-based symmetric capacitor has better conductivity in KOH and H_2SO_4 than in Na_2SO_4, which should be a result of the higher ionic conductivity of H^+ and OH^- in H_2SO_4 and KOH electrolytes. With respect to cycle stability, the GPC-based symmetric capacitor is relatively stable in the three electrolytes, especially in KOH, benefiting from its interconnected hierarchical porosity for the effective transfer of charges/electrons in pores.

Based on the above analysis, it is believed that H_2SO_4 electrolyte is suitable for small capacitors with a high capacitance and a long cycle life. If a high energy density and a large working voltage are required for aqueous symmetric capacitors, Na_2SO_4 electrolyte can be considered to be a better selection. The GPC electrode shows good overall electrochemical performance in KOH, and has wide applications in aqueous supercapacitors. If a high-capacitance, low-resistance and long-life aqueous supercapacitor is required, KOH electrolyte is the first choice.

4. Conclusions

In summary, we report a simple, sustainable and effective one-step strategy to construct highly graphitized porous carbon with a high proportion of micropores, an ideal graphitic skeleton and well-interconnected micro–meso–macropore size distribution. In this synthesis, K_2FeO_4 acts as both an activating agent and graphitization catalyst to achieve the synchronous hierarchical pore-formation and graphitization. Benefiting from the unique structural features combining high micropore surface area, superior conductivity and multiscale pore size distribution, the resultant GPC material presents an outstanding electrochemical capacitive performance in various aqueous electrolytes. Meanwhile, we established the relationship between the structure of GPC and electrochemical capacitive performance in different aqueous electrolytes, which would provide a valuable reference for GPC-based supercapacitors in different practical applications. We believe that our proposed strategy can provide a new direction for large-scale utilization

© 2022 The Author(s). Published by the Royal Society of Chemistry

Open Access Article. Published on 12 January 2022. Downloaded on 1/21/2026 7:43:06 PM.
This article is licensed under a Creative Commons Attribution-NonCommercial 3.0 Unported Licence.

and conversion of biomass to engineer highly capacitive carbons in high-performance energy storage applications.

Conflicts of interest

There are no conflicts to declare.

Acknowledgements

This work was supported by the National Natural Science Foundation of China (51872110), Science and Technology Project of Henan Province (212102210127), Natural Science Foundation of Education Department of Henan Province (21B150011), the special fund project of Zhengzhou Basic and Applied Basic Research (ZZSZX202001, ZZSZX202002 and ZZSZX202101), and the Undergraduate Training Program for Innovation of Henan Province (S202111834002, S202111834008, and S2021118340011).

References

1 W. L. Zhang, R. Guo, J. Sun, L. Q. Dang, Z. H. Liu, Z. B. Lei and Q. J. Sun, *J. Colloid Interface Sci.*, 2019, **553**, 705–712.
2 W. L. Zhang, R. Guo, L. Q. Dang, J. Sun, Z. H. Liu and Z. B. Lei, *J. Power Sources*, 2021, **507**, 230303.
3 L. Borchardt, M. Oschatz and S. Kaskel, *Mater. Horiz.*, 2014, **1**, 157–168.
4 S. J. Song, F. W. Ma, G. Wu, D. Ma, W. D. Geng and J. F. Wan, *J. Mater. Chem. A*, 2015, **3**, 18154–18162.
5 M. Y. Song, Y. H. Zhou, X. Ren, J. F. Wan, Y. Y. Du, G. Wu and F. W. Ma, *J. Colloid Interface Sci.*, 2019, **535**, 276–286.
6 B. B. Chang, L. Wang, W. W. Shi, Y. T. Chai, S. R. Zhang and B. C. Yang, *Sustainable Energy Fuels*, 2020, **4**, 2527–2540.
7 S. M. Liu, Y. R. Liang, W. Zhou, W. Q. Hu, H. Q. Hu, H. W. Dong, M. T. Zheng, H. Hu, B. F. Lei, Y. Xiao and Y. L. Liu, *J. Mater. Chem. A*, 2018, **6**, 12046–12055.
8 L. X. Dong, W. C. Li, B. Jiang, Y. Q. Zhou and A. H. Lu, *J. Mater. Chem. A*, 2019, **7**, 687–692.
9 B. B. Chang, Y. L. Wang, K. M. Pei, S. M. Yang and X. P. Dong, *RSC Adv.*, 2014, **4**, 40546–40552.
10 C. Largeot, C. Portet, J. Chmiola, P. L. Taberna, Y. Gogotsi and P. Simon, *J. Am. Chem. Soc.*, 2008, **130**, 2730–2731.
11 C. Liu, X. Yan, F. Hu, G. Gao, G. Wu and X. Yang, *Adv. Mater.*, 2018, **30**, 1705713.
12 D. W. Wang, F. Li, M. Liu, G. Q. Lu and H. M. Cheng, *Angew. Chem., Int. Ed.*, 2008, **120**, 379–382.
13 Y. N. Gong, D. L. Li, C. Z. Luo, Q. Fu and C. X. Pan, *Green Chem.*, 2017, **19**, 4132–4140.
14 F. Niu, R. Guo, L. Q. Dang, J. Sun, Q. Li, X. X. He, Z. H. Liu and Z. B. Lei, *ACS Appl. Energy Mater.*, 2020, **3**, 7794–7803.
15 S. Dutta, A. Bhaumik and K. C. W. Wu, *Energy Environ. Sci.*, 2014, **7**, 3574–3592.
16 C. Nita, M. Bensafia, C. Vaulot, L. Delmotte and C. M. Ghimbeu, *Carbon*, 2016, **109**, 227–238.
17 B. B. Chang, Y. Z. Guo, Y. C. Li, H. Yin, S. R. Zhang, B. C. Yang and X. P. Dong, *J. Mater. Chem. A*, 2015, **3**, 9565–9577.
18 H. Pei, G. F. Ma, K. J. Sun, J. J. Mu, Z. Zhang and Z. Q. Lei, *ACS Appl. Mater. Interfaces*, 2014, **6**, 20795–20803.
19 C. Shi, L. Hua, J. Hou, K. Guo, T. Zhai and H. Li, *Energy Storage Mater.*, 2018, **15**, 82–90.
20 J. Chmiola, G. Yushin, Y. Gogotsi, C. Portet, P. Simon and P. L. Taberna, *Science*, 2006, **313**, 1760–1763.
21 Z. M. Chen, X. F. Wang, Z. Y. Ding, Q. L. Wei, Z. C. Wang, X. M. Yang and J. S. Qiu, *ChemSusChem*, 2019, **12**, 5099–5110.
22 T. S. Wang, S. Y. Hu, D. Wu, W. W. Zhao, W. Yu, M. Wang, J. Xu and J. H. Zhang, *J. Mater. Chem. A*, 2021, **9**, 11839–11852.
23 W. J. Liu, K. Tian, Y. R. He, H. Jiang and H. Q. Yu, *Environ. Sci. Technol.*, 2014, **48**, 13951–13959.
24 J. C. Wang and S. Kaskel, *J. Mater. Chem.*, 2012, **22**, 23710–23725.
25 Y. Shen, *J. Mater. Chem. A*, 2015, **3**, 13114–13188.
26 M. Sevilla and A. B. Fuertes, *Carbon*, 2006, **44**, 468–474.
27 Q. Wang, J. Yan, Y. B. Wang, T. Wei, M. L. Zhang, X. Y. Jing and Z. J. Fan, *Carbon*, 2014, **67**, 119–127.
28 L. Zhang, M. J. Zhang, Y. H. Wang, Z. L. Zhang, G. W. Kan, C. G. Wang, Z. Y. Zhong and F. B. Su, *J. Mater. Chem. A*, 2014, **2**, 10161–10168.
29 G. X. Wang, J. Yang, J. Park, X. L. Gou, B. Wang, H. Liu and J. Yao, *J. Phys. Chem. C*, 2008, **112**, 8192–8195.
30 L. Bokobza, J.-L. Bruneel and M. Couzi, *Chem. Phys. Lett.*, 2013, **590**, 153–159.
31 C. J. Chen, J. W. Song, S. Z. Zhu, Y. J. Li, Y. D. Kuang, J. Y. Wan, D. Kirsch, L. S. Xu, Y. B. Wang, T. T. Gao, Y. L. Wang, H. Huang, W. T. Gan, A. Gong, *et al.*, *Chem*, 2018, **4**, 544–554.
32 W. Li, Z. J. Chen, H. P. Yu, J. Li and S. X. Liu, *Adv. Mater.*, 2021, **33**, 2000596.
33 S. Ikeda, K. Tachi, Y. H. Ng, Y. Ikoma, T. Sakata, H. Mori, T. Harada and M. Matsumura, *Chem. Mater.*, 2007, **19**, 4335–4340.
34 D. Yu, Y. Ma, M. Chen and X. Dong, *J. Colloid Interface Sci.*, 2019, **537**, 569–578.
35 H. Chen, T. Liu, J. Mou, W. Zhang, Z. Jiang, J. Liu, J. Huang and M. Liu, *Nano Energy*, 2019, **63**, 103836.
36 F. T. Ran, X. B. Yang, X. Q. Xu, S. W. Li, Y. Y. Liu and L. Shao, *Chem. Eng. J.*, 2021, **412**, 128673.
37 R. Zhang, X. Jing, Y. Chu, L. Wang, W. Kang, D. Wei, H. Li and S. Xiong, *J. Mater. Chem. A*, 2018, **6**, 17730–17739.
38 J. Zhao, Y. Jiang, H. Fan, M. Liu, O. Zhuo, X. Wang, Q. Wu, L. Yang, Y. Ma and Z. Hu, *Adv. Mater.*, 2017, **29**, 1604569.
39 W. W. Shi, B. B. Chang, H. Yin, S. R. Zhang, B. C. Yang and X. P. Dong, *Sustainable Energy Fuels*, 2019, **3**, 1201–1214.
40 B. B. Chang, W. W. Shi, S. C. Han, Y. N. Zhou, Y. X. Liu, S. R. Zhang and B. C. Yang, *Chem. Eng. J.*, 2018, **350**, 585–598.
41 M. P. Bichat, E. Raymundo-Pinero and F. Beguin, *Carbon*, 2010, **48**, 4351–4361.
42 W. Yang, W. Yang, L. Kong, A. Song, X. Qin and G. Shao, *Carbon*, 2018, **127**, 557–567.
43 Y. Sun, J. J. Xue, S. Y. Dong, Y. D. Zhang, Y. F. An, B. Ding, T. F. Zhang, H. Dou and X. G. Zhang, *J. Mater. Sci.*, 2020, **55**, 5166–5176.

© 2022 The Author(s). Published by the Royal Society of Chemistry

Open Access Article. Published on 12 January 2022. Downloaded on 1/21/2026 7:43:06 PM.
This article is licensed under a Creative Commons Attribution-NonCommercial 3.0 Unported Licence.

44 J. Du, H. J. Lv, Y. Zhang and A. B. Chen, *ChemElectroChem*, 2021, **8**, 2028–2033.
45 A. Ariharan, K. Ramesh, R. Vinaygamoorthi, M. S. Rani, B. Viswanathan, S. Ramaprabhu and V. Nandhakumar, *J. Energy Storage*, 2021, **35**, 102185.
46 Z. R. Ying, Y. Z. Zhang, X. M. Lin, S. J. Hui, Y. X. Wang, Y. B. Yang and Y. C. Li, *Chem. Commun.*, 2020, **56**, 10730–10733.
47 J. Shao, M. Song, G. Wu, Y. Zhou, J. Wan, X. Ren and F. Ma, *Energy Storage Mater.*, 2018, **13**, 57–65.
48 N. Jackel, P. Simon, Y. Gogotsi and V. Presser, *ACS Energy Lett.*, 2016, **1**, 1262–1265.
49 Z. M. Chen, X. F. Wang, B. C. Xue, Q. L. Wei, L. H. Hu, Z. C. Wang, X. M. Yang and J. S. Qiu, *ChemSusChem*, 2019, **12**, 1390–1400.
50 C. Zhong, Y. Deng, W. Hu, J. Qiao, L. Zhang and J. Zhang, *Chem. Soc. Rev.*, 2015, **44**, 7484–7539.
51 L. Chen, X. Zhang, H. Liang, M. Kong, Q. Guan, P. Chen, Z. Wu and S. Yu, *ACS Nano*, 2012, **6**, 7092–7102.
52 L. Sun, C. Tian, M. Li, X. Meng, L. Wang, R. Wang, J. Yin and H. Fu, *J. Mater. Chem. A*, 2013, **1**, 6462–6470.
53 B. J. Gang, F. Zhang, X. L. Li, B. Zhai, X. Y. Wang and Y. Song, *J. Energy Storage*, 2021, **33**, 102132.
54 H. Q. Wang, X. Li, J. M. Peng, Y. Z. Cai, J. T. Jiang and Q. Li, *Nanoscale Adv.*, 2021, **3**, 4858–4865.

© 2022 The Author(s). Published by the Royal Society of Chemistry